Department of Physics and Astronomy
University of Heidelberg

Bachelor Thesis in Physics
submitted by

Christian Sonnabend

born in Wiesbaden (Germany)

Oktober 2020

On the influence of temperature-dependent η/s on transverse-momentum particle spectra in heavy-ion collisions

This Bachelor Thesis has been carried out by Christian Sonnabend at the
Physikalisches Institut der Universität Heidelberg
under the supervision of
Prof. Dr. Silvia Masciocchi

Abstract

Particle production in heavy-ion collisions has been studied in the last decade using relativistic hydrodynamics for the evolution of an exotic state of matter called quark-gluon plasma.
In this thesis, a recent code-implementation for the fluid dynamic evolution called Fluidum was used to examine the influence of the temperature-dependent transport coefficient called "shear viscosity over entropy" (η/s) on transverse-momentum particle spectra for pions, kaons and protons in the 0-5% centrality class.
In earlier works, a constant model for η/s was implemented and matched data up to $\chi^2_{red} = 1.37$ for five centrality classes.

In the first part of the analysis in this thesis, a variety of functional forms for η/s was implemented in Fluidum including a temperature dependent model obtained from Yang-Mills calculations to study their effect on particle spectra. In particular the influence of the high and low temperature region of this temperature dependent functional form was studied.
The second part of the analysis deals with a grid search along the parameters A (scaling-factor of η/s), τ_0 (starting time of hydrodynamic evolution), $(\zeta/s)_{max}$ (maximum of the bulk viscosity over entropy ratio), $norm$ (normalization of the initial entropy-density) and T_{fo} (freeze-out temperature) to find their best-fit values for the implemented temperature dependent and temperature independent η/s. Both functional forms were then compared.

Zusammenfassung

Die Entstehung von Teilchen in Schwerionenkollisionen sowie die zeitliche Entwicklung des Quark-Gluonen Plasmas wurde in jüngerer Forschung mithilfe der relativistischen Hydrodynamik untersucht. In dieser Arbeit wird ein kürzlich entstandenes Codepaket namens Fluidum verwendet um den Einfluss des temperaturabhängigen Transport-Koeffizienten "Scheerviskosität (geteilt durch Entropiedichte)" (η/s) auf p_T-Spektren für Pionen, Kaonen und Protonen in der '0-5% centrality class' zu untersuchen.
In früheren Studien wurde bereits eine konstante (temperaturunabhängige) Funktion für η/s untersucht und ein best-fit von $\chi^2_{red} = 1.37$ für fünf 'centrality classes' gefunden.

Der erste Teil der Analyse in dieser Arbeit wird sich mit der Untersuchung verschiedener funktionaler Abhängigkeiten für η/s und deren Einfluss auf die simulierten Spektren widmen. Unter den verwendeten Modellen befindet sich unter anderem auch eine best-fit Kurve aus der Yang-Mills Theorie. Insbesondere wurde der Einfluss der Hoch- und Tieftemperaturregionen auf die Spektren analysiert.

Der zweite Teil dieser Arbeit beschäftigt sich dann mit einer Grid-Suche entlang der Parameter A (Skalierungsfaktor für η/s), τ_0 (Startzeitpunkt der hydrodynamischen Beschreibung), $(\zeta/s)_{max}$ (Maximum der Bulk-Viskosität geteilt durch die Entropiedichte), $norm$ (Normalisierungsfaktor für die Entropiedichte) und T_{fo} (Freeze-Out Temperatur) um deren best-fit Wert für das temperaturabhängige und das temperaturunabhängige Modell für η/s zu finden. Beide Funktionen für η/s konnten dann verglichen werden.

Table of Contents

1 | Introduction

High-energy relativistic hadron collisions at accelerators like the LHC and RHIC create regions of very high energy-density and temperature, the quark-gluon plasma (QGP), resembling the conditions shortly after the big bang or in cores of neutron stars. It is of high scientific interest to study the QGP because fundamental assumptions about the underlying theoretical description of quantum chromodynamics can be tested.
The QGP exists only for a short period of time and in a small region of space, making it inaccessible for direct measurements. However what can be measured are emerging charged particles. Theoretical models can then be compared to final distributions of particles, from which properties of the QGP can be inferred.

1.1 Quarks, gluons and the QGP

Quarks and gluons, called partons, are the fundamental building blocks of matter in the universe and are subject to a quantum field theory called quantum chromodynamics (QCD). While quarks are the particles that make up the matter, gluons are the bosons carrying the strong force between them.
Quarks and gluons have a property called "color charge" which comes in three flavors (red, green and blue). Color-charged particles are not observed independently in nature, hence the concept of confinement was introduced. Confinement limits the possible arrangements of quarks to color-neutral hadronic states, such as mesons (quark-antiquark pair) and baryons (three quarks which make a color-neutral binding), out of which atoms are composed. Most prominent examples of baryons are protons (p) and neutrons (n) and of mesons are pions (π) and kaons (K).

The principle of confinement is mathematically introduced by the strong coupling α_S. It describes the interaction strength between quarks and ensures that a separation of quarks at ordinary energy densities, which are confined in a hadronic state,

would require such high energies that a new quark-antiquark pair would be produced from the vacuum. Hence, the quarks would still remain in color-neutral states [1]. A visual representation of this phenomenon is shown in figure 1.1 (left), where a $q\bar{q}$-pair (quark-antiquark pair) is split apart and recombines with a new $q\bar{q}$-pair produced from the vacuum.

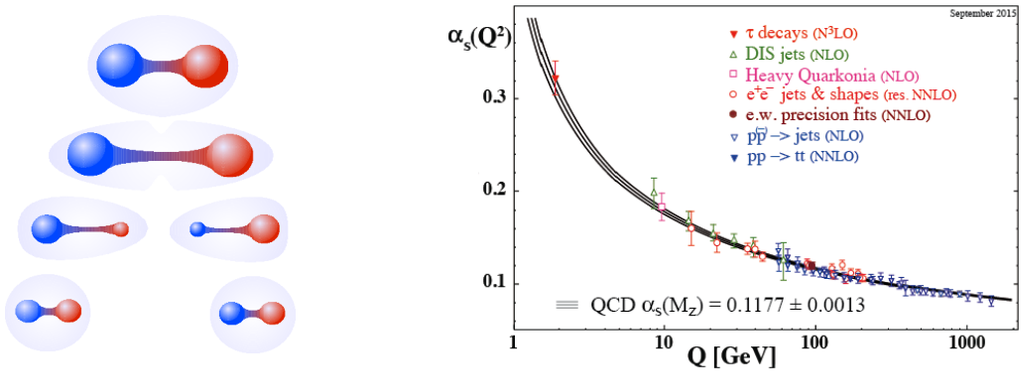

Figure 1.1: Left figure[1]: Quarks remain in color-neutral states by creating a $q\bar{q}$-pair
Right figure [2] : Strong coupling α_S in dependence of momentum-transfer

However, at sufficiently high energy-densities, α_S is small. Quarks and gluons can then move independently without being confined [3]. This property is called "asymptotic freedom".

As it can be seen on figure (1.1) (right) α_S falls monotonously for higher momentum exchanges (Q) between two interacting particles. High energy densities, like the ones created in heavy-ion collisions, lead to high momentum exchanges between the constituent hadrons. A system containing many subatomic particles, like two heavy ions (e.g. 2 Pb ions: $2 \cdot 82 = 164$ interacting baryons), can therefore create a deconfined state of matter which is dominated by almost freely moving quarks and gluons when brought to collision at velocities close to the speed of light. This state of matter is called quark-gluon plasma (QGP) [4].

[1]Image-source: https://webific.ific.uv.es/web/sites/default/files/QCD-confinement.png

1.2 Evolution of a heavy-ion collision

There are several stages which occur after a heavy-ion collision. A representation of those stages is shown in figure (1.2).

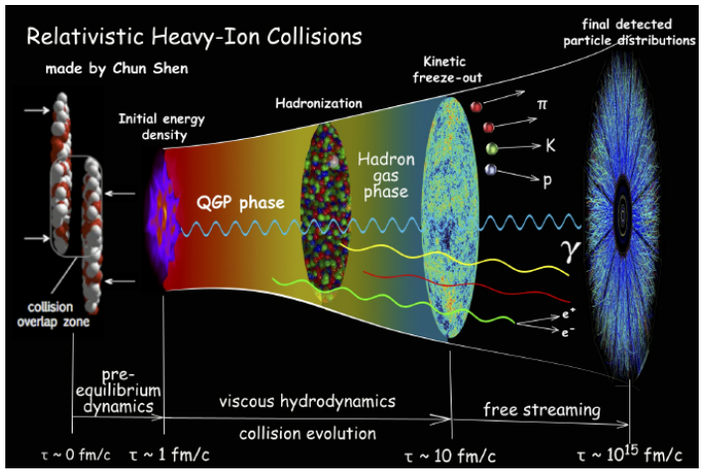

Figure 1.2: Representation of the evolution of a heavy-ion collision [2]. The horizontal axis is representative of the time axis.

As two nuclei collide at $\tau = 0$ fm/c (τ being the proper time in the reference frame of the nuclei, c the speed of light and 1 fm = 10^{-15} m), they interact according to their initial distribution of nucleons. A pair of interacting nucleons collides with an energy $\sqrt{s_{NN}}$ with typical values of 2.76 TeV for heavy-ion collisions at colliders like the Large Hadron Collider (LHC), producing particles in highly inelastic momentum-exchanging processes. In this region of high energy-density a deconfined, out-of-equilibrium state [5] of quarks and gluons is created.

The system thermalises quickly ($\tau \lesssim 1$fm/c, [6]). This was realized by a data-to-model comparison of integrated particle yields using the "statistical hadronisation model" [7, 8]. Thermodynamic quantities such as temperature, energy density or pressure can be used in a well defined way. A locally equilibrated, strongly coupled plasma emerges, the quark-gluon plasma.

[2]Image source: https://cpb-us-w2.wpmucdn.com/u.osu.edu/dist/f/4868/files/2014/09/little_bang-10wt2pd.jpg

Due to partonic interactions pressure gradients develop across the QGP [9], the system expands rapidly lowering the temperature and energy density.

The local thermal and chemical equilibration of the system as well as the strong coupling of partons allow a fluid dynamic treatment of the evolution of the QGP. Fluid dynamics is an elegant approach to circumvent the impossible description of all single-particle processes by only utilizing macroscopic quantities such as the energy-density or the pressure of the system.
The realization that fluid dynamics could be applicable to the evolution of the QGP was supported when a data-to-model comparison of particle spectra, in particular elliptic flow, was conducted and showed good agreement [10]. The analysis showed further that the QGP could be an almost perfect liquid, strengthening the assumption of a strongly coupled fluid.

In proximity of the critical temperature predicted by Lattice-QCD calculations ($T_{crit} = (156.5 \pm 1.5)$ MeV) [11, 12] around $\tau \approx 10$ fm/c, the degrees of freedom change from partonic to hadronic, meaning that α_S gets large enough for the quarks and gluons to recombine to mesons and baryons. This process is called "hadronization" [13], the fluid evolves into a "hadron resonance gas".

Eventually the system gets too dilute to maintain equilibrium, the fluid dynamic description is not applicable anymore.
Processes of particle production (chemical freeze-out) and momentum transfer (kinetic freeze-out) cease at $\tau \approx 20$ fm/c [14]. Particles move freely from there on but resonance decays are still possible. It is still topic of research whether chemical and kinetic freeze-out happen at the same temperature or whether there is an evolution of the system between chemical and kinetic freeze-out.

Final hadron distributions are then measured in detectors such as ALICE at the LHC at $\tau \approx 10^{15}$ fm/c [15]. Detectors like ALICE can measure transverse-momentum particle spectra with unprecedented precision which will also be used in this analysis (see chapter 3). Fits to data, as they will be done in this thesis, are only possible because of this precision.

2 | Relativistic Hydrodynamics

2.1 Ideal relativistic hydrodynamics

After the initial hadronic collision at $\tau = 0$ fm/c, the matter reaches a phase of high energy densities (ε) of approximately $\varepsilon \gtrsim 12$ GeV/fm^3, which corresponds to ≈24 times the typical hadron energy-density of ~ 0.5 GeV/fm^3 [16]. This stage of the evolution cannot be described using models such as fluid dynamics since it is far away from local thermal and chemical equilibrium. However, it was hypothesized that local equilibrium is reached rather quickly ($\tau \sim 1 - 2$ fm/c) due to strong microscopic dynamics. This leads to a fluid dynamic description of the strongly coupled plasma [17].

In ideal relativistic fluid dynamics, the evolution of a fluid is determined by the energy-momentum tensor $T^{\mu\nu} = T^{\mu\nu}(\varepsilon, u^\mu)$ and the evolution equations derived from its conservation law, when no other conserved charges such as e.g. baryon number are present.

The following definitions will be used in the equations:

- $\hbar = k_B = c = 1$, where $\hbar = h/2\pi$ is Planck's constant, k_B the Boltzmann-constant and c the speed of light
- The metric $g_{\mu\nu} = diag(-1, 1, 1, 1)$ for Cartesian coordinates in Minkowski space
- The fluid velocity in the Landau-frame u^μ
- The projector in the spacial part $\Delta^{\mu\nu} := g^{\mu\nu} + u^\mu u^\nu = diag(0, 1, 1, 1)$
- The covariant derivative d_μ, $\nabla^\mu = \Delta^{\mu\nu} d_\nu$

In local thermal equilibrium the energy-momentum tensor can be expressed using the four-velocity u^μ in the co-moving frame to the fluid velocity, the so called Landau frame, the metric $g_{\mu\nu}$, and the thermodynamic expressions for the pressure (p) and energy-density (ε) [9, 18] which are connected through the equation of state [19]:

$$T^{\mu\nu} = \varepsilon u^\mu u^\nu + p(g^{\mu\nu} + u^\mu u^\nu) \tag{2.1}$$

Considering a fluid with no other conserved charges like e.g. baryon number, the evolution of fluid fields (e.g. energy density ε and fluid velocity u^μ) is governed by the equations of motion which can be derived from the conservation of energy and momentum:

$$\nabla_\mu T^{\mu\nu} = 0 \tag{2.2}$$

Predictions of ideal fluid dynamics did not match elliptic flow data for non-central collisions at low energies [20]. In non-central collisions, the overlap region of the two colliding heavy-ions is anisotropic. Pressure gradients of different magnitude develop over the QGP which directly relate to momentum anisotropies in the final momentum distribution of hadrons. These momentum anisotropies were not explainable using ideal hydrodynamics. The description was modified by expanding the energy-momentum tensor in gradients. Dissipative deviations were include in terms of viscosities (first-order gradient expansion) and relaxation times (second-order gradient expansion).
The first-order expansion will be discussed in the next section to motivate the research on the viscosities.

2.2 Dissipative terms and first-order gradient expansion

The gradient expansion of the energy-momentum tensor can in general be written as [9]

$$T^{\mu\nu} = T^{\mu\nu}_{ideal} + \Pi^{\mu\nu} \tag{2.3}$$

where $T^{\mu\nu}_{ideal}$ is the form of the EM-tensor presented in (2.1) and $\Pi^{\mu\nu}$ is term which contains all gradients.

This decomposition can be expanded for a general symmetric EM-tensor by introducing two terms, the bulk viscous pressure π_{bulk} and the shear-stress tensor $\pi^{\mu\nu}$, which allows to split the EM-tensor into a parallel and orthogonal part to the fluid velocity u^μ

$$T^{\mu\nu} = \varepsilon u^\mu u^\nu + p(g^{\mu\nu} + u^\mu u^\nu) + \Pi^{\mu\nu} = \varepsilon u^\mu u^\nu + (p + \pi_{bulk})\Delta^{\mu\nu} + \pi^{\mu\nu} \tag{2.4}$$

This defines the deviation from the ideal energy momentum tensor as $\Pi^{\mu\nu} = \pi_{bulk}\Delta^{\mu\nu} + \pi^{\mu\nu}$.

There are two constraints that need to be fulfilled for $\pi^{\mu\nu}$:

1. The fluid velocity is defined as the time-like eigenvector to the energy-momentum tensor in the Landau-frame with the energy density being the corresponding eigenvalue $u_\mu T^{\mu\nu} = -\varepsilon u^\nu$. Therefore one must require $u_\mu \pi^{\mu\nu} = 0$
2. The bulk-viscous pressure π_{bulk} is defined as the trace of the viscous corrections $\Pi^{\mu\nu}$ which makes the shear-stress tensor traceless by definition $Tr(\pi) = \pi^\mu_\mu = 0$.

First order approximations of $\pi^{\mu\nu}$ and π_{bulk} can be calculated as [9]

$$\pi_{bulk} = -\zeta \nabla_\mu u^\mu \tag{2.5}$$

$$\pi^{\mu\nu} = \eta(T)\left(\Delta^{\mu\alpha}\Delta^{\nu\beta}(\nabla_\alpha u_\beta + \nabla_\beta u_\alpha - \frac{2}{3}\Delta_{\alpha\beta}\nabla \cdot u)\right) := -\eta\sigma^{\mu\nu} \tag{2.6}$$

The functions ζ (bulk viscosity) and η (shear viscosity), called transport coefficients, quantify the transport of momentum through the fluid. The viscosities determine microscopic momentum exchanges and hence the first-order dissipative deviations from an ideal fluid.
A physical interpretation of the bulk viscous pressure π_{bulk} can be given as the pressure arising from the bulk viscosity and the shear-stress tensor $\pi^{\mu\nu}$ as the contribution to the pressure from the shear viscosity transverse to the fluid velocity [9].

Using the equation for the energy and momentum conservation (2.2) with the modified energy-momentum tensor (2.3), the fluid dynamic equations of motion can be calculated explicitly [21]

$$\begin{aligned} &\text{I) } u^\mu \partial_\mu \varepsilon + (\varepsilon + p + \pi_{bulk}) \nabla_\mu u^\mu + \pi^{\mu\nu} \nabla_\mu u_\nu = 0 \\ &\text{II) } (\varepsilon + p + \pi_{bulk}) u^\mu \nabla_\mu u^\nu + \nabla^\nu (p + \pi_{bulk}) + \Delta^\nu_\alpha \nabla_\mu \pi^{\mu\alpha} = 0 \end{aligned} \tag{2.7}$$

First order viscous hydrodynamics can however lead to acausal propagations. Second order gradient expansions of the energy-momentum tensor are possible and topic of current research. However the theory behind this goes beyond this primary introduction.

2.2.1 Entropy production

The viscosities describe deviations from an ideal fluid and quantify microscopic momentum transfer. A viscous fluid will produce entropy.
In the absence of conserved charges such as e.g. the baryon number and corresponding chemical potentials, the entropy density (s) can be written as a function of the pressure p, the temperature T and the energy density ε of the system using the first law of thermodynamics [9]

$$DE = T \cdot DS - p \cdot DV \quad \Rightarrow \quad \frac{DE}{DV} + p = T \frac{DS}{DV} \quad \Leftrightarrow \quad \varepsilon + p = sT \tag{2.8}$$

where $D := u^\mu d_\mu$ is the projection along the fluid velocity u^μ, E the energy, S the entropy and V the volume of the system.

Using this relation and exploiting the fact that there is an equation of state [19] which relates temperature and pressure, the first order equations of motion can be applied to calculate an expression for the production of entropy within each fluid element.

Using the equations of motion for an ideal fluid (2.7, setting $\pi_{bulk} = 0$ and $\pi^{\mu\nu} = 0$), the following equation can be calculated

$$Ds = \frac{1}{T} \cdot D\varepsilon = \frac{1}{T} \cdot u^\mu \partial_\mu \varepsilon = -s \nabla_\mu u^\mu \tag{2.9}$$

Rewriting this equation directly yields the conservation of entropy for an ideal fluid

$$u^\mu \nabla_\mu s = -s \nabla_\mu u^\mu \quad \Rightarrow \quad \nabla_\mu (s u^\mu) = 0 \tag{2.10}$$

This calculation can be done again using the first order equations of motion which include viscosities (2.7). The equations for entropy production from η and ζ can be obtained

$$\begin{aligned} \frac{Ds}{s} &= -\nabla_\mu u^\mu - \frac{1}{sT}(\pi_{bulk} \nabla_\mu u^\mu + \pi^{\mu\nu} \nabla_\mu u_\nu) \\ &= -\nabla_\mu u^\mu - \frac{1}{sT}(\pi_{bulk} \Delta^{\mu\nu} + \pi^{\mu\nu}) \nabla_\mu u_\nu \\ &= -\nabla_\mu u^\mu - \frac{1}{sT} \Pi^{\mu\nu} \nabla_\mu u_\nu \end{aligned} \tag{2.11}$$

The first term can be identified with the expression for the ideal fluid, while the second term describes the contribution from the inclusion of viscosities. Entropy is not conserved anymore.
When substituting with the expressions for π_{bulk} and $\pi^{\mu\nu}$ one finds that shear and bulk viscosity only appear in their dimensionless form η/s and ζ/s and are directly proportional to the entropy production. Furthermore, since $Ds \geq 0$ by the second law of thermodynamics one finds $\eta/s \geq 0$ and $\zeta/s \geq 0$ [21].
Shear and bulk viscosity are therefore important fluid properties that govern the first-order dissipative deviations from an ideal fluid. Increasing the transport coefficients can therefore lead to an increase in entropy and enhanced particle production.

2.3 Transport coefficients

Finding suitable expressions for the transport coefficients is a great theoretical challenge since they are difficult to determine directly from analytic quantum field theory.
In the high temperature regime perturbation theory calculations are applicable, since α_S is small and can be used as an expansion parameter. However, theoretical calculations face problems at temperatures close to the QCD critical temperature. One being that the degrees of freedom change, another being the fact that perturbative calculations are not applicable anymore since α_S gets too large to be used as an

expansion parameter.
One way the transport coefficients can be determined analytically is by using Kubo-relations [22, 23] which are calculated as a linear, first-order response to an excitation of a fluid. This was done in [24] for pure Yang-Mills theory. Resulting errors from the theoretical calculations are fitted by an analytic fit-function.
For phenomenological studies, fit functions for the transport coefficients are well suited, since they are inspired by first principles and capture the physical behavior for different temperature regimes. One possible fit-funtion for $\eta/s(T)$ [24] was used in this thesis to evaluate its influence on transverse-momentum particle spectra calculated with a code-framework called Fluidum. The main ideas behind this temperature depend model for η/s and the functional form used for ζ/s will be presented here.

2.3.1 Shear viscosity over entropy density

Past works on η/s calculated that in a class of theories which contain gravity duals (AdS/CFT correspondence) a lower bound for η/s can be set to $1/(4\pi)$ [25]. For all known substances today, this lower bound holds [26, 27]. By analyzing elliptic flow data it was conjectured that η/s has a value close to this lower bound [28]. Temperature independent models for η/s were investigated in various hydrodynamic simulations [29, 30].

Since theoretical calculations such as the pure Yang-Mills calculations have small remaining errors, a global fit function for η/s was conjectured in [24] by superposing two different functional dependencies for their specific temperature regimes above and below the critical temperature.

At high temperatures ($T >> T_C$), the fluid is dominated by partonic degrees of freedom and perturbation theory is applicable since α_S is small. In the analysis of [24] it was found that a good description of the hard thermal loop (HTL) resumed data [31] in the high temperature regime is given by

$$\frac{\eta}{s}(\alpha_s) = \frac{a}{\alpha_s^{\gamma}} \tag{2.12}$$

where α_s describes the strong coupling as mentioned in the introduction and a, γ are fit parameters of the function. The functional form of α_s in this high temperature

regime was calculated from a heavy quark potential, which rises linearly at large distances

$$\alpha_{s,HQ}(z) = \frac{1}{\beta_0}\frac{z^2-1}{z^2 ln(z^2)} \tag{2.13}$$

where $z = cT/T_C$ is a dimensionless momentum variable with fit-parameter c and β_0 is given in Yang-Mills theory as $\beta_0 = 33/(12\pi)$.

For the low temperature region ($T << T_C$), a HRG model was considered for which a power-law behavior of η/s is expected [32]. The global fit-function was designed as the sum of both

$$\frac{\eta}{s}(T) = \frac{a}{\alpha^{\gamma}_{s,HQ}(cT/T_C)} + \frac{b}{(T/T_C)^{\delta}} \tag{2.14}$$

where a, b, c, γ and δ are fit-parameters evaluated from a fit to the Yang-Mills calculations. This functional dependence forms the main body of analysis in this work. Figure (2.1) shows the temperature dependence of the above mentioned model (2.14) for the parametrization given in the paper [24] for a critical temperature of $T_C = 156$ MeV.

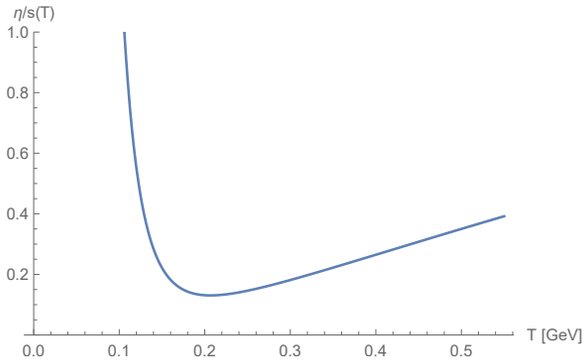

Figure 2.1: Plot of the temperature dependent model for η/s in a range of T $\in [0, 0.55]$ GeV. The parameters are given in the paper [24] as $a = 0.15$, $b = 0.14$, $c = 0.66$, $\gamma = 1.6$, $\delta = 5.1$. The critical temperature was set close to the result of Lattice QCD at $T_C = 156$ MeV.

During the time of writing this thesis, a new parametrization was introduced by Jan Pawlowski et al. which was used in this thesis[1]. In a private conversation it was discussed that this new parametrization was obtained from new Yang-Mills results,

but a scaling-coefficient A could be introduced to the function since the overall normalization was not fixed by the calculation. The new parametrization in comparison to the old parametrization are shown below in figure (2.2). The parameters of the two curves are given in table (2.1).

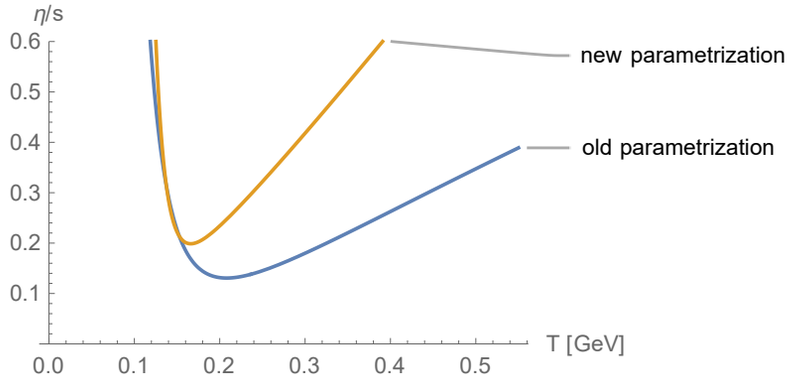

Figure 2.2: Comparison of the old and new parametrization for the temperature dependent model for η/s. The curve with the new parametrization was plotted with a scale-factor of $A = 1$.

	a	b	c	γ	δ
param. in paper	0.15	0.14	0.66	1.6	5.1
new param.	1.55339	0.0500256	0.205005	1.09023	10.3999

Table 2.1: Parametrization of the temperature dependent model for η/s. Comparison of the parametrization given in the paper [24] and the new parametrization.

2.3.2 Bulk viscosity over entropy density

After the discussion of the model for η/s it is also necessary to review main aspects which influence the temperature dependent models of the bulk-viscosity over entropy ζ/s.

The physical picture behind the bulk viscosity (ζ) is a transport coefficient changing with the volume of the fluid. Hence, for macroscopic, non-compressible fluids it can

[1]hrefhttps://archiv.ub.uni-heidelberg.de/volltextserver/28503/https://archiv.ub.uni-heidelberg.de/volltextserver/28503/

be shown that the bulk viscosity is zero. The transport coefficients (viscosities) in heavy ion collision are however affected by a crossover from partonic to hadronic degrees of freedom at the critical temperature. It is therefore conjectured that the bulk viscosity models this phase transition with a non-zero value around the critical temperature [33].

A first model for the bulk viscosity was proposed to have an exponential shape for the two temperature regimes [34], while further analysis assumed a fit function using a Lorentzian shape [35]. The Lorentzian shape, modified by an extra hyperbolic tangent to bring ζ/s to 0 for $T \to 0$ which ensures causality, was used in [29] and will also be used for this thesis.

$$\zeta/s = tanh(|20 \cdot T|) \cdot \frac{(\zeta/s)_{max}}{1 + \left(\frac{T - T_{peak}}{\Delta T}\right)^2} \tag{2.15}$$

Other models are possible and worth further investigation. The functional form is plotted in the following figure.

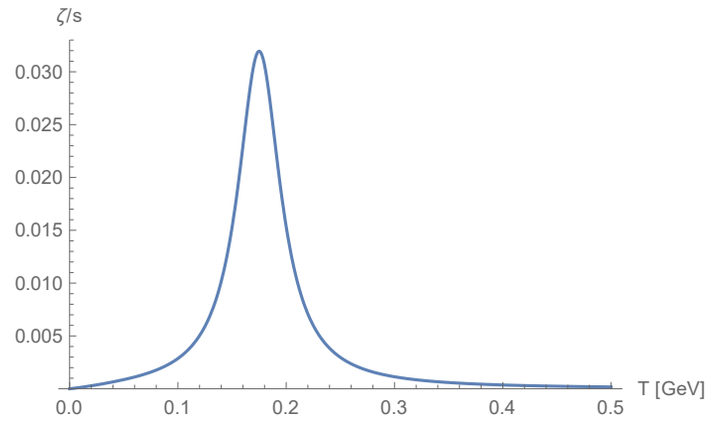

Figure 2.3: $\zeta/s(T)$ plotted against the temperature with $(\zeta/s)_{max} = 0.032$, $T_{peak} = 0.175$ GeV, $\Delta T = 0.024$ GeV

3 | Fluidum

In this chapter, the basic ideas behind the fluid dynamic simulation tool Fluidum and how its results are compared to measured data will be presented.

3.1 Coordinate system

In order to solve the equations of motion presented in the last chapter, it is convenient to choose an adapted coordinate system which accounts for symmetries and simplifies mathematical calculations.

A coordinate system which is suited for solving the fluid dynamic equations of motion in relativistic nuclear collisions can be constructed by introducing, the Bjorken time τ and the rapidity η and using cylindrical coordinates in the plane transverse to the beam axis (x-y plane). The Bjorken time can be constructed as $\tau = \sqrt{t^2 - z^2}$ from the time t in the laboratory frame and the z-coordinate along the beam axis. It measures the proper time in the frame of reference of a particle. The rapidity is defined as $\eta = arctanh(z/t)$. In combination, these two variables specify the location along the z-axis and the time since the initial nuclear collision occured. Cylindrical coordinates are well suited for the transverse plane. The azimuthal angle $\varphi = arctan(y/x)$ which corresponds to the angle enclosed between the direction of motion of the particle and the x-axis, and the radial distance from the beam axis $r = \sqrt{x^2 + y^2}$ are used to specify locations in the transverse plane.
Furthermore, transverse momentum can now be defined as the momentum of a particle in the transverse plane. In Cartesian coordinates, this corresponds to $p_T = \sqrt{p_x^2 + p_y^2}$ where p_x and p_y are the x- or y-component of the momentum.

3.2 Fluidum

Fluidum is a code package written in Mathematica to solve the equations of motion of second order gradient expansions of the EM-tensor, using numerical methods for the partial differential evolution equations (PDEE) and mode expansions for the solutions. For detailed explanations and formulas I refer to [21].

Fluid fields such as the temperature, the fluid velocity, the bulk viscous pressure or components of the shear-stress tensor are collected in the "Nambu spinor" $\mathbf{\Phi}$ (N dimensional vector) and can be written in general by splitting them into azimuthally-symmetric (symmetry in φ) and Bjorken-boost (symmetry in η) invariant background fields $\mathbf{\Phi}_0(\tau, r)$ representing the part of fields which can be thought of as an expectation value, and fluctuations $\mathbf{\Phi}_1(\tau, r, \varphi, \eta)$ which cause event-by-event deviations from the background.

$$\mathbf{\Phi}(\tau, r, \varphi, \eta) = \mathbf{\Phi}_0(\tau, r) + \epsilon \mathbf{\Phi}_1(\tau, r, \varphi, \eta) \tag{3.1}$$

The parameter ϵ is an expansion parameter which allows to split the evolution equations for the background and fluctuating part. For the final solution, the parameter needs to be set to $\epsilon \to 1$.

The fluid evolution is guided by a set of hyperbolic, quasi-linear partial differential equations (PDEE) and can be written in a symbolic form as

$$\mathbf{A}\left(\mathbf{\Phi}, \tau, r\right)\cdot\partial_\tau\mathbf{\Phi} + \mathbf{B}\left(\mathbf{\Phi}, \tau, r\right)\cdot\partial_r\mathbf{\Phi} + \mathbf{C}\left(\mathbf{\Phi}, \tau, r\right)\cdot\partial_\varphi\mathbf{\Phi} + \mathbf{D}\left(\mathbf{\Phi}, \tau, r\right)\cdot\partial_\eta\mathbf{\Phi} - \mathbf{S}\left(\mathbf{\Phi}, \tau, r\right) = 0 \tag{3.2}$$

where $\mathbf{A}$, $\mathbf{B}$, $\mathbf{C}$, $\mathbf{D}$ are (N×N) matrices and $\mathbf{S}$ an N-dimensional vector [21].
By inserting the full form of $\mathbf{\Phi}$ (3.1) into the PDEE (3.2), the evolution equations can be separated by the order of ϵ. The equation resulting from zeroth order in ϵ is the evolution equation for the unperturbed background fields $\mathbf{\Phi}_0$.
Symmetry arguments allow an easier calculation of the background fields by reducing the number of independent components and the dimensionality of the PDEE. The parameter ϵ is therefore useful since the background and fluctuation part can be evolved independently.

For the work in this thesis, only the evolution of the background fields was considered, because the results of the hydrodynamic simulation is compared to azimuthally averaged transverse momentum particle spectra in the mid-rapidity region.

3.2.1 Initial conditions

The background fields evolve by the equations of relativistic viscous hydrodynamics. In order to solve the equations numerically, initial conditions need to be specified. The initial conditions of the background fields are specified on a Cauchy-surface of constant Bjorken time τ_0.

Initial conditions for the calculations in this thesis were used from a previous analysis done in [29] which utilized an initial state model called Trento [36] providing a radial profile for the initial entropy density. The process of calculating this initial entropy density in Trento should be briefly discussed here. For this, the concept of centrality classes is introduced shortly. For a detailed explanation I refer to [37] and [36].

3.2.2 Centrality classes

Centrality classes quantify how central a collision between two nuclei occured. This is measured by the impact parameter b describing the distance between the centers of the two colliding nuclei in the transverse plane. The fundamental assumption why centrality classes can be assigned is that the impact parameter is monotonically related to the particle multiplicity, i.e. the number of produced particles per collision. Central collisions, i.e. low impact parameter, produce high multiplicities. Experimentally, the multiplicity of charged particles (N_{ch}) per event can be measured. Centrality classes can be defined over the fraction of the total integral of the distribution dN_{evt}/dN_{ch} as [37, 38]

$$\frac{\int_{\infty}^{n_i}(dN_{evt}/dN_{ch})dN_{ch}}{\int_{\infty}^{0}(dN_{evt}/dN_{ch})dN_{ch}} = i \tag{3.3}$$

where n_i is the boundary for the i percentile of the centrality class. For example, the 10-20% centrality class would be defined by the boundaries n_{10} and n_{20} as

$$\frac{\int_{\infty}^{n_{10}}(dN_{evt}/dN_{ch})dN_{ch}}{\int_{\infty}^{0}(dN_{evt}/dN_{ch})dN_{ch}} = 0.1 \quad and \quad \frac{\int_{\infty}^{n_{20}}(dN_{evt}/dN_{ch})dN_{ch}}{\int_{\infty}^{0}(dN_{evt}/dN_{ch})dN_{ch}} = 0.2 \tag{3.4}$$

3.2.3 Trento

The initial conditions as they are calculated in Trento [36] should now be discussed. In a heavy-ion collision, the two nuclei A and B overlap to a certain extend. The extend to which they overlap is characterized by the density of nuclear matter which participates in inelastic collisions $\rho_{A,B}^{part}(x,y,z)$. The participant thickness for each nucleus is calculated as

$$T_{A,B}(x,y) = \int \rho_{A,B}^{part}(x,y,z)dz \tag{3.5}$$

The primary assumptions are that entropy is produced if a collision occurs, and there exists a function $f(T_A, T_B)$ converting the participant thicknesses into entropy at mid-rapidity and at the thermalization time τ_0 [36]. The function $f(T_A, T_B)$ is proposed to be

$$f(T_A,T_B) = T_R(p;T_A,T_B) = \left(\frac{T_A^p + T_B^p}{2}\right)^{1/p} \tag{3.6}$$

where p is called the reduced thickness parameter. The entropy per unit rapidity produced in a collision is then proportional to the transverse density $T_R(p;T_A,T_B)$

$$\frac{dS}{dy} \propto T_R(p;T_A,T_B) \tag{3.7}$$

which was implemented in the analysis performed in [29] as

$$s(r) = \frac{norm}{\tau_0}\langle T_R(r,\varphi)\rangle \tag{3.8}$$

A central collision produces a higher entropy density than a peripheral collision due to higher number of binary nucleon-nucleon collisions. The integrated transverse density $\int T_R(\vec{x})d^2x$ is monotonously related to the charged particle multiplicity which can be used to divide the simulated events into centrality classes. For each centrality class the entropy density can then be calculated and is determined up to a normalization factor. The normalization-factor will be used as a fit parameter later on.

The initial entropy profile, together with thermodynamic relations and the equation of state is used in Fluidum to initialize the temperature T, the fluid velocity u^μ, the bulk viscous pressure π_{bulk} and two components of the shear-stress tensor $\pi^{\eta\eta}$, $\pi^{\phi\phi}$.

Initial radial flow is neglected by setting $\pi^{\eta\eta} = \pi^{\phi\phi} = \pi_{bulk} = 0$ at the beginning of the evolution.

The initial conditions for the calculations in Fluidum were generated from one Trento event as an average over 10^5 independent simulated events [29]. In particular the reduced-thickness parameter $p = 0$ was used which corresponds to $T_R = \sqrt{T_A T_B}$, the geometric mean of T_A and T_B.

3.2.4 Calculation of spectra

The process of hadronization is implemented in Fluidum by utilizing the Cooper-Frye calculation at the freezeout-temperature T_{fo} [39]. Using an appropriate particle distribution function f_a (modified Bose-Einstein or Fermi-Dirac distributions for particle species a), the energy of the particle in the fluid rest-frame $\bar{E}_{\mathbf{p}} := -u^\nu p_\nu$ and an appropriately chosen Cauchy surface Σ of constant temperature, the Cooper-Frye formulation gives an expression for particle distributions of species a on the Cauchy surface as

$$E_{\mathbf{p}} \frac{d^3 N_a}{d^3 \mathbf{p}} = \frac{\nu_a}{(2\pi)^3} \int_\Sigma f_a(\bar{E}_{\mathbf{p}}) p^\mu d\Sigma_\mu \tag{3.9}$$

The particle distribution function of an ideal fluid can be expressed in terms of Bose-Einstein (BE) or Fermi-Dirac (FD) statistics, but additional particle production has to be accounted for due to the shear-stress tensor $\pi^{\mu\nu}$ and the bulk-viscous pressure π_{bulk}. These deviations from an ideal BE- or FD-distribution are accounted for by including corrections δf^{bulk} and δf^{shear}.

$$f = f_{eq} + \delta f^{bulk} + \delta f^{shear} \tag{3.10}$$

Explicit expressions for δf^{bulk} and δf^{shear} can be found in [40], the equilibrium term f_{eq} is given by BE or FD distributions.

Resonance decays can further impact the spectra and particle ratios. They are implemented in Fluidum by utilizing decay maps (decay kernels) which convert sufficiently unstable particles in two and three body decays. The decay kernels can be

calculated with an openly available code called FastReso [41] and were taken for this analysis from the analysis done in [29]. This is implemented in the code by applying the decay maps before evaluating the integral in (2.9) which has the advantage that unstable particles are not evolved until after the freeze-out. Roughly 700 resonance decays were used from a 2016 Particle Data Group publication [42].

Results of this calculation are transverse momentum spectra of the form $(d^2N/(2\pi p_T dp_T dy))$ which are evaluated for all sufficiently stable particle species (such as e.g. π, K or p) and produce spectra values for a given list of p_T values.

4 | Analysis & Results

The temperature dependent functional form for η/s was implemented in Fluidum. Spectra obtained from Fluidum with a constant and a temperature dependent η/s are compared with experimental results measured by the ALICE collaboration [43].

4.1 Analysis techniques

4.1.1 The Alice Data

The data used for this analysis are transverse momentum particle spectra from Pb-Pb collisions for π, K and p obtained from the 2010 run at $\sqrt{s_{NN}} = 2.76$ TeV at the LHC, measured by the ALICE collaboration [43]. The experimental spectra are given in the form $1/N_{ev}(d^2N/(2\pi p_T dp_T dy))$ (y is the rapidity, N_{ev} is the number of collisions measured for the entire run) in units of $[c^2/\text{GeV}^2]$ in dependence of the transverse momentum p_T in units of $[\text{GeV}/c]$.
What can be seen in figure (4.1) is the average number of particles per event, measured at mid-rapidity ($|y| < 0.5$). The data was scaled by a factor ($\times 10^n$) for each centrality for better visibility.

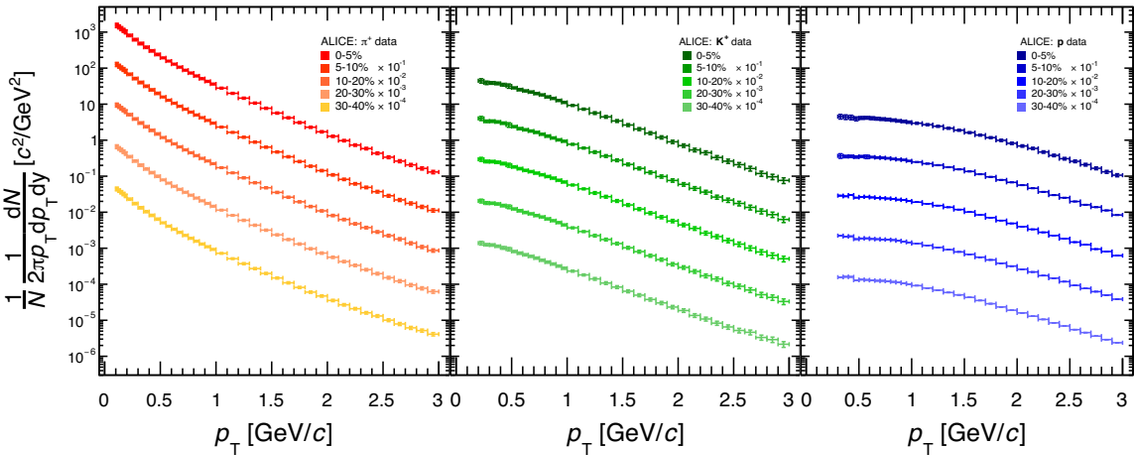

Figure 4.1: Transverse-momentum particle spectra measured in Pb-Pb collisions with the ALICE detector in 2010 at $\sqrt{s_{NN}} = 2.76$ TeV for Pions (left), Kaons (middle) and Protons (right) [43].

For the analysis in this thesis only the data from the 0-5% centrality class, i.e. very central collisions, will be used.

One remark which has to be made about this data is that the p_T-intervals for π, K and p are not perfectly identical. While the π data is already measured for p_T-intervals of 0.1 GeV/c, K start at 0.2 GeV/c and p at 0.3 GeV/c. This is due to different detectors and their specific analysis techniques being used. For a detailed explanation I refer to [43].
Since Fluidum evaluates the spectra at a given list of p_T values, the p_T-intervals of the ALICE data were imported to Fluidum. This makes the calculated spectra of Fluidum directly comparable to the experimental data. All p_T-lists were imported up to $p_T = 3$ GeV/c.

4.1.2 Grid search

A temperature dependent functional form for η/s as presented in the previous chapter and a temperature independent form for η/s will be investigated. The ability of a certain functional form for η/s to describe data can be evaluated by finding best-fit values for parameters and comparing the calculated spectra to the experimentally measured data. Similar to the analysis in [29], the following parameters are used as

fit parameters

- $norm$: The normalization factor for the initial entropy density
- $(\zeta/s)_{max}$: The maximum of the bulk viscosity
- τ_0: The initialization time of the fluid dynamic evolution
- T_{fo}: The temperature of the freeze-out surface
- η/s: The scaling parameter of η/s for the temperature dependent functional form or the constant value for a temperature independent functional form

Identical to the analysis in the paper [29], no distinction between chemical and kinetic freeze-out was made. A freeze-out surface of constant temperature T_{fo} is used.

In order to find best fit values for the above mentioned parameters, a grid-search method is performed. The grid-search uses a fixed number of points in a fixed range of values for each of the parameters. In this way the phase-space spanned by the parameters and their corresponding ranges is divided into equally spaced points. For each point in this five-dimensional hypercube, corresponding to one parameter configuration of the form [$norm$, η/s, $(\zeta/s)_{max}$, τ_0, T_{fo}], the spectra can be evaluated using Fluidum. These spectra can then be compared to data.

The goodness of fitting the data-points is evaluated using the statistical χ^2_{red} function.

$$\chi^2_{red} = \frac{1}{N_{dof}} \sum_{i=0}^{N} \frac{(x_i - y_i)^2}{\sigma_i^2} \tag{4.1}$$

Where x_i describes a data-point at some given p_T-value, y_i the spectrum-value produced by Fluidum at this p_T-value and σ the uncertainty for the data-point which is in turn given by $\sigma_i = \sqrt{\sigma^2_{i,sys} + \sigma^2_{i,stat}}$. The sum is evaluated for each data-point, i.e. for three particle species (π, K, p) and their specific number of p_T-intervals $N^a_{p_T}$ for particle species a, from the experimental data [43] (N^{π}_{pT}=41, N^{K}_{pT}=36, N^{p}_{pT}=34). The number of degrees of freedom N_{dof} can then be calculated as $N_{dof} = N^{\pi}_{p_T} + N^{K}_{p_T} + N^{p}_{p_T}$ - #(fit parameters) $= 111 - 5$.
A good fit to data would ideally produce a value of $\chi^2_{red} = 1$, while worse fits raise the value of χ^2_{red}.

What results from the grid calculation is a "pixelated surface" of the beneath lying χ^2_{red}-landscape. An example of how a "pixelated" χ^2_{red}-landscape in this grid looks like is presented in figure (4.2). The colors indicate the χ^2_{red} at the given grid point. What can be seen in this example are two dimensional subspaces of parameters to see how the landscape looks like around a minimum

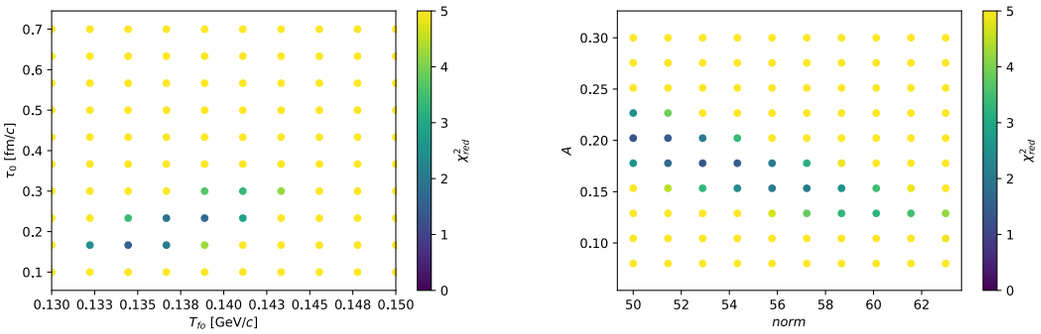

Figure 4.2: Visual representations of the χ^2_{red}-landscape around a minimum. The pictures show plots along the parameters T_{fo} & τ_0 and $norm$ & η/s. The picture is only meant as an illustration.

4.1.3 Splining the χ^2_{red}-landscape & finding minima

In order to find a local or possibly global minimum in the χ^2_{red}-landscape, it is necessary to interpolate between the grid points. This was done in this analysis using a splining algorithm in combination with an optimzier to find minima which is provided by a framework called Minuit [44].

The grid-points are not connected by any direct functional relation, hence in between two grid points a polynomial function of a given, maximal order (n) is chosen to connected them. The resulting function connecting all points is called an n^{th}-order spline.
Certain conditions must be fulfilled when two polynomials meet at a grid point in order to guarantee continuity and differentiability of the n-th order spline, e.g. for an n-th order spline it is usually demanded that the spline is $(n-1)$ times continuously differentiable at each grid point. Due to the piece wise definition between the grid points the polynomials are more flexible than a single polynomial interpolation across all grid points and can accommodate for stronger fluctuations while still maintaining a smooth and $(n-1)$-times differentiable course.

When the grid-points are connected by n-th order splines, the migrad-optimizer of the Minuit package [44] can find a minimum by using an inexact line-search method. An initialization point and an initial step width have to be specified. If multiple minima exist in the χ^2_{red}-landscape, the initialization and the order of the spline used to interpolate the landscape can have an influence on the location of the minimum found by migrad.
Uncertainties on the parameters of the found minimum are evaluated with the tool minos [44]. It accounts for non-linearities in the splined landscape and parameter correlations. The uncertainties of the parameters are evaluated using the χ^2-landscape. If the profiles of the minima in the χ^2-landscape found by the migrad optimizer are approximately of gaussian shape, the uncertainties of the parameters can be evaluated by finding the range in each dimension for which the value of χ^2 increases by 1 compared to the minimum ($\chi^2_{min} + 1$) [44].

4.2 Systematic studies on η/s

4.2.1 Results of a previous analysis

In a recent publication [29], a grid search was conducted for a temperature independent model for η/s for 5 centrality classes (0-5%, 5-10%, 10-20%, 20-30%, 30-40%). The normalization-factor for the initial entropy density was considered as an independent parameter for each centrality class. The parameter ranges for each centrality class were divided in equidistant points which results in 10^5 configurations calculated for each of the five centrality classes. The grid was calculated within the ranges given in table (4.1).

$norm_i$	η/s	$(\zeta/s)_{max}$	τ_0 [fm/c]	T_{fo} [MeV]
50 - 67	0.08 - 0.25	0.005 - 0.1	0.1 - 0.6	130 -150

Table 4.1: Parameter-ranges for the grid run with η/s=const. done in the paper [29]. The index i indicates that the normalization was chosen as an independent parameter in each centrality class.

The best-fit values for the 0-5% centrality found in the fit using 5 centrality classes are stated in table (4.2). Data was reproduced up to a $\chi^2_{red} = 1.37$. However it must be kept in mind that these parameters result from a fit for all five centrality classes and do not necessarily represent the best-fit parameters if only the 0-5% centrality class was used for a fit. The uncertainties on the parameters are the result of the minos analysis tool.

$norm_{0-5}$	η/s	$(\zeta/s)_{max}$	τ_0 [fm/c]	T_{fo} [MeV]
54.2±0.6	0.164±0.007	0.059±0.003	0.179±0.005	137.1±0.3

Table 4.2: Best-fit values as found in the analysis in [29] for a nine dimensional grid.

In the analysis of the paper another grid run had been performed using only the 0-5% centrality class (rather than five centrality classes). The optimization of this grid resulted in the values stated in table (4.3).

	$norm_{0-5}$	η/s	$(\zeta/s)_{max}$	τ_0 [fm/c]	T_{fo} [MeV]
result	51.9±2.0	0.197±0.027	0.081±0.013	0.175±0.014	136.2±0.8

Table 4.3: Best-fit values from the analysis done in [29] using only the 0-5% centrality class.

The 1σ-intervals of the minimum found in the grid using five centralities and the minimum found when only centrality is used overlap. This allows to use the results of the fit to five centrality classes for further qualitative discussions.

Comparison with the results of the paper

As discussed in the previous chapter, a different way of calculating the χ^2 values was used in this thesis in comparison to the analysis done in the paper [29]. In this thesis, the particle spectra were computed along the p_T-lists of the given experimental data which makes the spectra values directly comparable to the experimental data. In the analysis of the paper, the spectra were calculated for a generic p_T-list of the form $p_T \in$ range(0.1,3.0,0.1) and the spectra were interpolated in order to be comparable to the experimental data. To compare how the new method of calculation with the Fluidum version used for this thesis can perform, an identical grid was calculated and the optimization procedure was applied. The result is shown in the table (4.4).

	$norm_{0-5}$	η/s	$(\zeta/s)_{max}$	τ_0 [fm/c]	T_{fo} [MeV]
result	52.6±0.8	0.190±0.008	0.077±0.004	0.177±0.012	136.3±0.4

Table 4.4: Best-fit values calculated from a grid run with the new Fluidum version using only the 0-5% centrality class.

It can be seen that the used version of the Fluidum and the new calculation technique can reproduce the previously found result (table (4.3)) within the 1σ range of the parameter uncertainties. The χ^2_{red}-value found for this configuration with the spline function was evaluated to 1.16. In order to confirm the χ^2_{red}-value found by the splines, a single direct computation of this parameter configuration was conducted and a value of $\chi^2_{red} = 1.19$ was found. Slight deviations in the χ^2_{red}-values could be explained by the splines that did not fit perfectly to the χ^2_{red}-landscape. However, the found minimum emphasizes that the results obtained in this analysis are compatible with the results obtained from the paper.

Low-p_T pion excess

Particle spectra for low-p_T pions are systematically underestimated by the Fluidum calculations. This effect was previously noticed in [29]. To illustrate this, the spectra were computed with the best-fit parameters from the fit with five centrality classes (see table (4.3)). In figure (4.3) it can be seen that the computed spectra can reproduce the measured data for kaons and protons very well, but pions are systematically underestimated by the calculation for $p_T < 0.5$ GeV/c. This effect can be seen in the following plot of the particle spectra for pions, kaons and protons in the 0-5% centrality class.

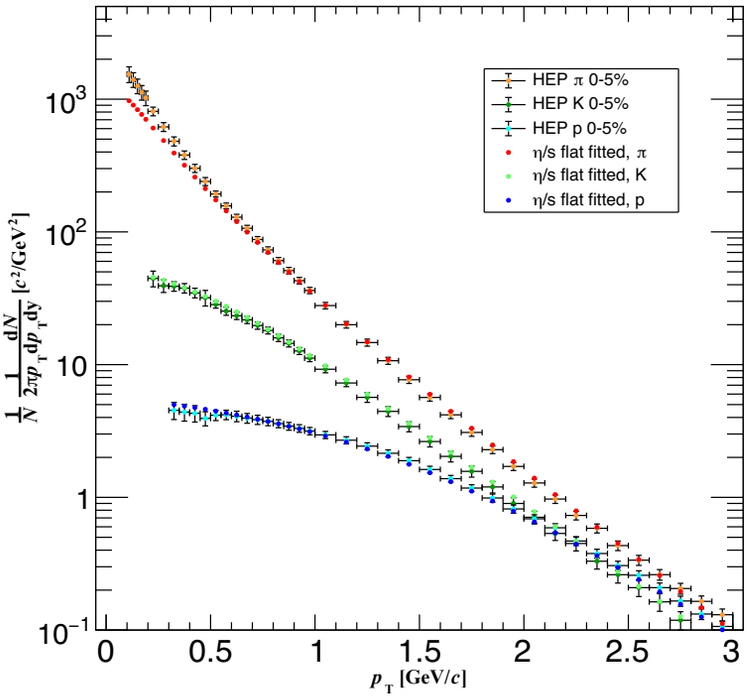

Figure 4.3: Calculated spectra from the configuration in table (4.2) and measured spectra of the ALICE data plotted for $p_T \in [0, 3.0]$ GeV/c for pions (red), kaons (green) and protons (blue).

This excess of pions in experimental data is even more visible when the calculated spectra are plotted as a ratio of the measured data. Errors are then calculated using the gaussian error propagation as $\Delta(x_i/y_i) = \Delta x_i/y_i$ where x_i is a data point of the

experimental data, Δx_i its error, y_i the corresponding calculated value ($\Delta y_i = 0$ since the computation is exact) and i the index which runs over all spectra values in figure (4.3). This results in the following ratio plots figure (4.4)

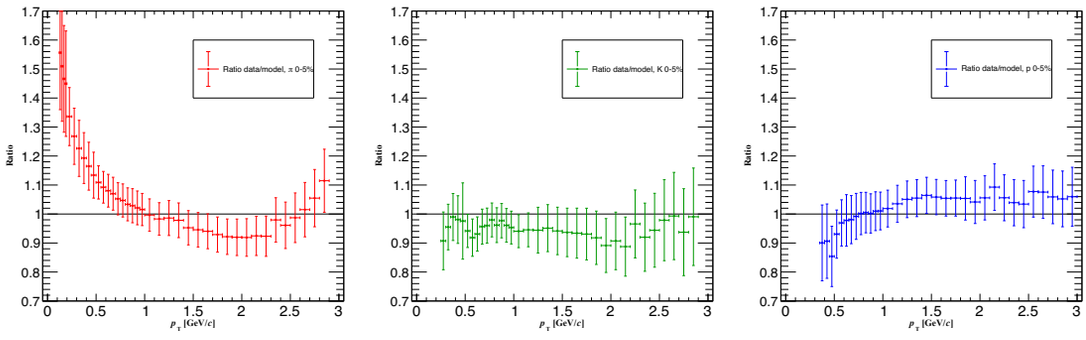

Figure 4.4: Ratio-plots of the spectra calculated with Fluidum to data for $p_T \in [0, 3.0]$ GeV/c for pions (red), kaons (green) and protons (blue) in the 0-5% centrality class. A clear pion excess at low p_T-values is apparent in the experimental data.

Kaons and protons are reproduced within their 1σ-intervals for almost all p_T-intervals. In the paper [29] this effect was analyzed and the low-p_T pions were excluded from the fit. It was found that the χ^2_{red}-value can be significantly lowered when the pion measurements at low p_T-intervals were excluded. A χ^2_{red}-value of 0.6 was then achieved.
Hence this pion excess artificially inflates the χ^2_{red}-value of a parameter configuration. It also indicates that there are unknown physical phenomena which are not yet included in the hydrodynamic simulations.

4.2.2 Investigating the temperature dependent η/s

Since there is no foreknowledge on how the temperature dependent η/s influences the calculated particle spectra, the best-fit values as presented in table (4.2) will be used to qualitatively investigate the influence of this temperature dependent functional form on particle spectra. The parametrization for the temperature dependent η/s as it was presented in the paper [24] and in table (2.1, first row) will be used. The spectra for pions in the 0-5% centrality class were compared. The two functional forms are shown in figure (4.5, left) together with the freeze-out temperature $T_{fo} = 137.1$ MeV. This freeze-out temperature marks the important temperature up

to which the transport coefficients are used in the calculation. On figure (4.5, right) the ratio of the calculated spectra for pions in the 0-5% centrality class is shown.

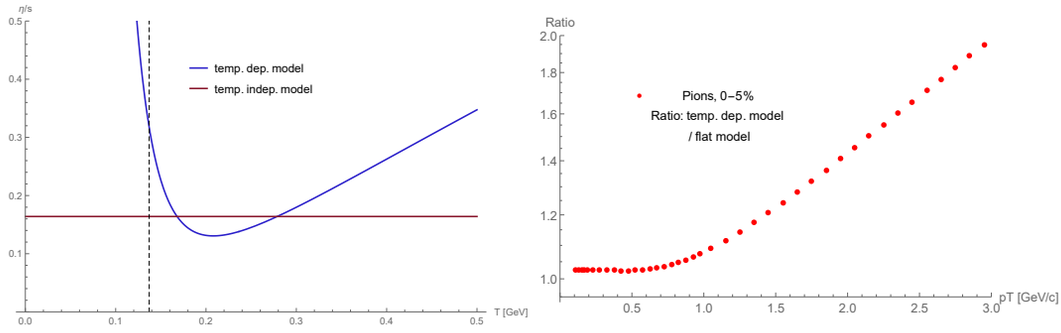

Figure 4.5: Left: Comparison of the two models for η/s.
Right: Ratio of calculated pion spectra in the 0-5% centrality class.

It can be noticed that the temperature dependent η/s results in higher particle multiplicities in all p_T-intervals. For high p_T-intervals, the particle mulitplicity is almost doubled while the functions produce similar multiplicities for low p_T-intervals. This result matches expectations since a higher value for η/s corresponds to stronger momentum transfers which leads to higher particle multiplicities.

With the parametrization for the temperature dependent η/s from the paper [24], shown in table (2.1, first row), η/s reaches a minimum at $T_{min} \approx 1.3T_C \approx 207$ MeV. It is a priori unknown how each temperature region (above and below the minimum) influences particle production. To investigate this, the temperature dependent model was set to a value of $\eta/s(T_{min}) \approx 0.131$ for I) $T > T_{min}$ and II) $T < T_{min}$.

$$\left(\frac{\eta}{s}\right)^{mod}_{\mathrm{I}}(T) = \begin{cases} \frac{\eta}{s}(T) & \text{for } T < T_{min} \\ \frac{\eta}{s}(T_{min}) \approx 0.131 & \text{for } T > T_{min} \end{cases} \tag{4.2}$$

and

$$\left(\frac{\eta}{s}\right)^{mod}_{\mathrm{II}}(T) = \begin{cases} \frac{\eta}{s}(T) & \text{for } T > T_{min} \\ \frac{\eta}{s}(T_{min}) \approx 0.131 & \text{for } T < T_{min} \end{cases} \tag{4.3}$$

The two models can be seen in figure (4.6)

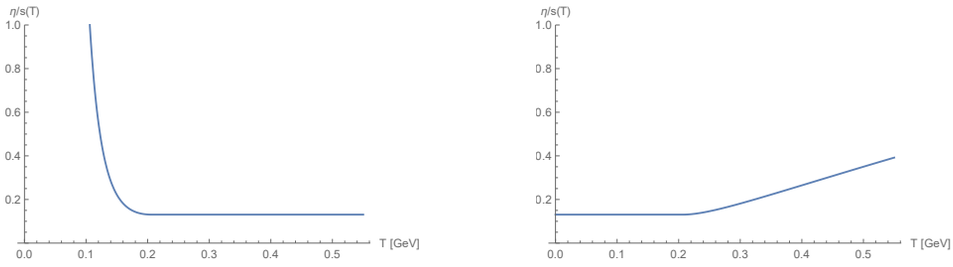

Figure 4.6: Plots of the functional variations of the temperature dependent η/s. Left: $(\eta/s)^{mod}_{\mathrm{I}}(T)$, Right: $(\eta/s)^{mod}_{\mathrm{II}}(T)$.

In order to investigate the particle production in these temperature regions, the spectra are computed for pions in the 0-5% centrality class with both variations of the temperature dependent functional form ((4.2) & (4.3)) as well as with the full temperature dependent functional form. The purpose of this test is to isolate the effects of the high and low temperature region and not to fit experimental data. Therefore all other parameters ($norm$, $(\zeta/s)_{max}$, τ_0, T_{fo}) were left unchanged for the calculations. The parameters as specified in table (4.2) from the fit to five centrality classes were used for this investigation. Ratios are then compared between the full temperature dependent η/s and the two modified versions of this functional form. The results can be seen in figure (4.7)

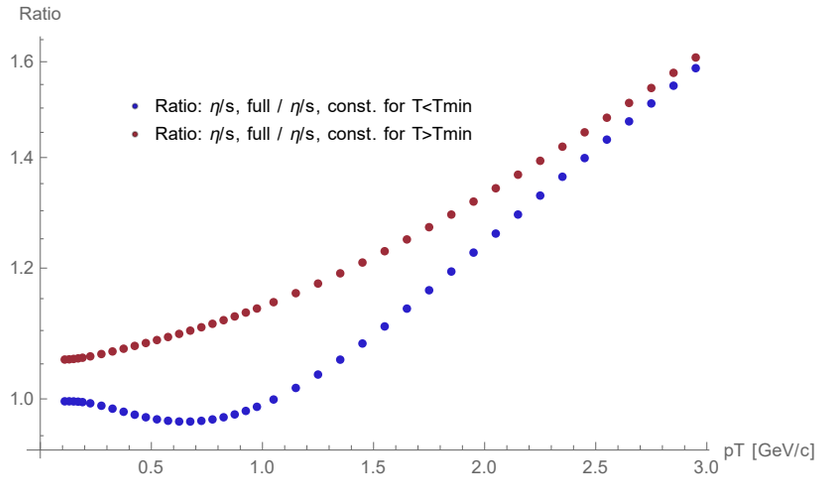

Figure 4.7: Ratios of the modified temperature dependent η/s to the full temperature dependent functional form.

Since all other parameters that enter the calculations of Fluidum were left identical for the calculation of the three computed spectra, the only influence on the ratios can come from the functional form for η/s.
The two ratios show that both the high and low-temperature part of the temperature dependent η/s seem to influence particle production at high p_T-intervals to a similar

amount in comparison to the full temperature dependent η/s. The low p_T-intervals seem to be influenced more by the high temperature regime of η/s since the ratio approaches unity for the modified version of η/s which was set to a constant value for $T < T_{min}$.

4.3 Exploring the χ^2-landscape

In order to compare the influence of the temperature dependent and the temperature independent functional form of η/s on particle spectra, best-fit values were found with the grid search method for $norm$, η/s, $(\zeta/s)_{max}$, τ_0 and T_{fo}. This also allows a comparison with the ALICE data by evaluating χ^2_{red} which quantifies the ability of a the different functional forms to fit the experimental data.

4.3.1 Temperature dependent η/s: A coarse grained grid

For the grid search with the temperature dependent η/s the new parametrization of the curve was used (see table 2.1, second row). As described before, this allows to introduce a scale-factor (A) to the curve since the overall normalization of this curve is not fixed by the theoretical calculations. The effect of scaling the curve is visualized in figure (4.8)

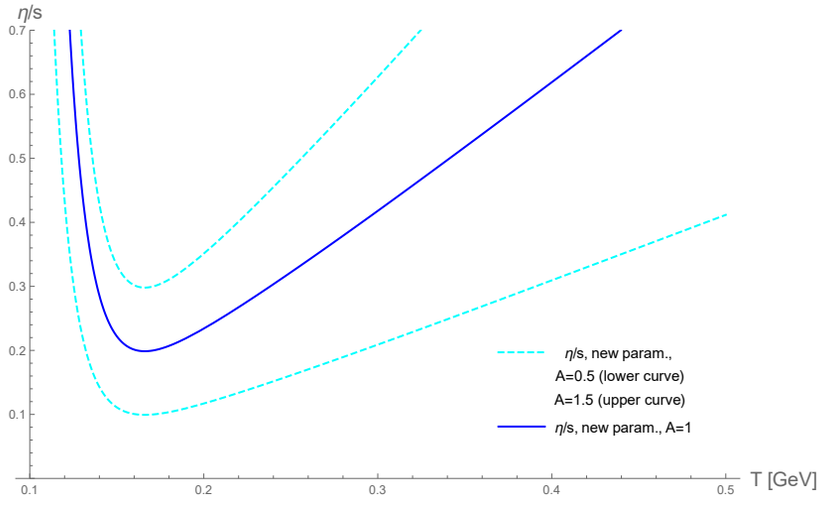

Figure 4.8: The cyan coloured curves indicate a scale factor of 1.5 (upper) or 0.5 (lower). The dark blue curve indicates the curve with a scale factor of 1.

As it can be seen, the scale factor can have a major influence on the slope and the location of the minimum of the curve. The minimum of the curve is found at

$T_{min} = 166$ MeV$\approx 1.06 T_C$. For $A = 1$ the curve approaches a value of $\eta/s(A = 1, T_{min}) \approx 0.2$.

In order to compare the scaled temperature dependent to the temperature independent functional form for η/s, optimal parameters for $norm$, A, $(\zeta/s)_{max}$, τ_0 and T_{fo} need to be computed.
Since there is no prior information about a set of parameters which can fit particle data best, i.e. the location of a minimum in the χ^2_{red}-landscape, a coarse grained grid was computed for this function. This allows a first estimation of the location of a minimum. The ranges for this coarse grained grid can be found in table (4.5).

	$norm$	A	$(\zeta/s)_{max}$	τ_0 [fm/c]	T_{fo} [MeV]
ranges	50 - 80	0.5 - 1.5	0.001 - 0.13	0.2 - 1.5	130 - 150

Table 4.5: Parameter-ranges for the first grid run with the temperature dependent η/s. 10 bins were used in each dimension.

The resulting χ^2-landscape from the grid calculation was then splined and the migrad optimizer was used to find a minimum. The minimum which was found is shown in table (4.6). The errors on the parameters were computed from the minos error analysis tool from the minuit package. A spline of order $n = 7$ was used to fit the χ^2-landscape and localize the minimum.

	$norm$	A	$(\zeta/s)_{max}$	τ_0 [fm/c]	T_{fo} [MeV]
found min.	56.1±0.85	0.90±0.06	0.083±0.007	0.399±0.015	136.8±0.5

Table 4.6: Results of the first grid run with the temperature dependent η/s.

The values of the spline-function at the given minimum can be evaluated to $\chi^2_{red,spline} = 1.13$. However, in order to validate the χ^2_{red}-value which was calculated from the splines, the according χ^2_{red}-value was computed in a single direct calculation using the parameters of the minimum. The result of this calculation was $\underline{\chi^2_{red,comp.} = 1.29}$. Seemingly, the splines produce a different value of χ^2_{red} for the found minimum. One explanantion for this underestimation of the χ^2_{red}-value could be that the grid ranges were chosen to coarse for the splines to accurately fit to the landscape. A finer grained grid was investigated to test this assumption.

It is however interesting to note that a reasonably good fit to data can be found for

a scale factor of $A = 0.9$. This corresponds to a minimum of the curve of ≈ 0.18 which is in proximity to the best-fit value which was found for the temperature independent η/s in the comparison to the results of the paper (see table (4.5)). Since the curve rises rather steeply around the minimum, the particle production from η/s is compensated by a larger τ_0 compared to previous the results from the paper (see table 4.3). This corresponds to a delayed start of the hydrodynamic evolution and a lower initial entropy density, since the initial entropy density is normalized by $norm/\tau_0$.
However, to get a more precise location of the minimum and a direct comparison between the temperature dependent and the temperature independent η/s a grid search along the same parameter ranges needs to be conducted for both models.

4.3.2 Temperature dependent η/s: A fine grained grid

In order to find an accurate minimum in the χ^2-landscape, a finer grained grid was computed for the temperature dependent η/s. This grid computation was designed to further investigate the location of a minimum in the landscape by reducing the ranges of the parameters. According to the minimum which was found in the previous grid, the ranges as in table (4.7) were used.

	$norm$	A	$(\zeta/s)_{max}$	τ_0 [fm/c]	T_{fo} [MeV]
ranges	50 - 63	0.5 - 1.0	0.02 - 0.1	0.1 - 0.7	130 - 150

Table 4.7: Parameter-ranges for the second grid run with the temperature dependent η/s. 10 bins were used in each dimension. The ranges were chosen according to the minimum found in the first grid search.

Again, an $n = 7$ order of splining the resulting χ^2-landscape was used. The initialization of the migrad optimizer was chosen with the best-fit parameters of the minimum found in the coarse grained grid. This revealed a minimum at the location given in table (4.8)

	$norm$	A	$(\zeta/s)_{max}$	τ_0 [fm/c]	T_{fo} [MeV]
result	54.7±0.98	0.73±0.06	0.074±0.008	0.325±0.016	137.3±0.5

Table 4.8: Best-fit values found in the second grid search with the temperature dependent η/s. 10 bins were used in each dimension.

The χ^2_{red}-value resulting from the splines is $\chi^2_{red,spline} = 1.21$, while a single, direct computation of this configuration resulted in $\underline{\chi^2_{red,comp.} = 1.25}$. The results of the coarse grained grid and the fine grained grid agree within 3σ. Deviations of the minima could be a result of the splines not capturing the landscape correctly for the coarse grained grid. As shown before for the coarse grained grid, the spline function underestimated the χ^2_{red}-value at the minimum. It was also found that a different initialization of the migrad optimizer can produce variations in the found minimum. This dependence is topic of current investigation. Nevertheless the configuration above produced the lowest χ^2_{red}-value found in a direct computation and should be discussed physically.

It can be seen that the scale factor for the temperature dependent η/s approaches a lower value than in the coarse grained grid. A slightly increased value for $(\zeta/s)_{max}$ enhances particle production during the hydrodynamic evolution phase and slightly compensates the lower value of η/s. A similar effect can be seen on the parameters τ_0 and $norm$. The parameter $norm$ stays similar for both configurations while τ_0 approaches lower values in the finer grid than in the coarse grained grid. This corresponds to a higher initial entropy density for the result in the fine grained grid since the normalization for the initial entropy density is given by $norm/\tau_0$. This means that entropy production and hence particle production from η/s is lower in the result of the finer grid and is compensated mainly by the higher initial entropy density.

4.3.3 Temperature independent η/s

From the results of the previous analysis done in [29], it was considered that a grid run using the parameter ranges from the fine grained grid of the temperature dependent η/s can also indicate the location of a minimum for the temperature independent η/s. This makes the results of the temperature dependent and the temperature independent functional form for η/s comparable to one another. For η/s the range was chosen in [0.08, 0.3]. The lower bound of this range is chosen as the AdS/CFT-boundary of $1/4\pi \approx 0.08$. The ranges are stated in table (4.9).

Using an n=7 spline function and initializing the migrad optimizer with the best-fit parameter configuration from the paper (see table 4.2) shows, that a minimum can be found at the location stated in table (4.10)

The resulting $\chi^2_{red,spline}$-value from the splines is $\chi^2_{red} = 1.14$, a direct computation

	$norm$	η/s	$(\zeta/s)_{max}$	τ_0 [fm/c]	T_{fo} [MeV]
ranges	50-63	0.08-0.3	0.02 - 0.1	0.1 - 0.7	130 - 150

Table 4.9: Parameter-ranges for the finer grained grid run with the temperature independent η/s. 10 bins were used in each dimension.

	$norm$	η/s	$(\zeta/s)_{max}$	τ_0 [fm/c]	T_{fo} [MeV]
result	52.6±0.7	0.197±0.008	0.080±0.003	0.185±0.010	136.3±0.4

Table 4.10: Best-fit values for the temperature independent η/s found in the finer grid. 10 bins were used in each dimension.

of this parameter configuration revealed a value of $\chi^2_{red,comp.} = 1.19$. The results are in overall good agreement with the results obtained from the previous grid run (see table 4.4). The uncertainties of the parameters overlap within the 1σ intervals for all parameters. For this grid it was also noticed that the order of the used spline can have an influence on the location of the minimum. However the variations in the minimum still allow a physical discussion of the results.

With the results of this grid both functional forms for η/s (temperature dependent and temperature independent) can now be compared.

4.3.4 Comparison of the results

Best-fit parameters were found for both functional forms. The results obtained from the χ^2-landscape and each single parameter-dimension can now be compared.

The two best-fit parameter configurations were found as seen in table (4.11)

model	$norm$	η/s / A	$(\zeta/s)_{max}$	τ_0 [fm/c]	T_{fo} [MeV]	χ^2_{red}
temp. ind.	52.6±0.7	0.197±0.008	0.080±0.003	0.185±0.010	136.3±0.4	1.19
temp. dep.	54.7±0.98	0.73±0.06	0.074±0.008	0.325±0.016	137.3±0.5	1.25

Table 4.11: Results of the two finer grid runs for the temperature dependent and the temperature independent model.

The temperature independent η/s reaches a slightly lower χ^2_{red}-value. Due to the imprecise estimation of the χ^2_{red}, the dependence of the minimum on the initializa-

tion of migrad and the order of the spline, no definite conclusion can be stated about which model can fit the experimental data better. It is rather the physical behavior within the parameters which can be investigated in order get insights on the effect of using the temperature dependent η/s.

For a first comparison, both functional forms were plotted with their best-fit values as stated in table (4.11) and can be seen in figure (4.9).

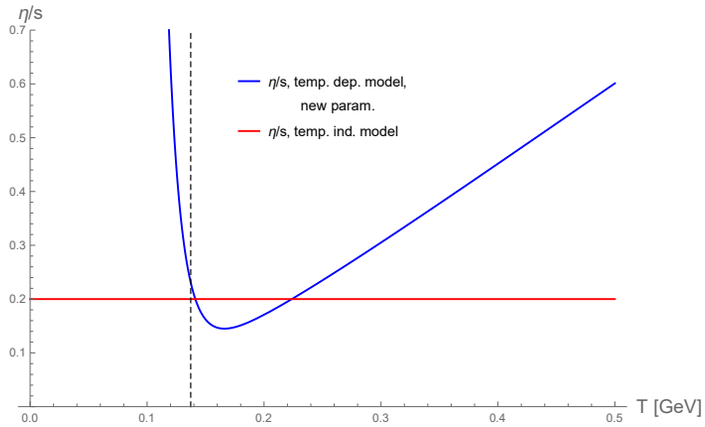

Figure 4.9: Plot for η/s in a temperature region of $T \in [0, 0.5]$ GeV. The dashed line indicates the temperature of the freeze-out surface found for the temperature dependent η/s.

As it can be seen on the plot, the temperature dependent η/s approaches a minimum below the temperature independent function. It reaches a minimum at $T_{min} = 166$ MeV with a value of $\eta/s(T_{min}) = 0.145$. The two functions for η/s intersect at $T_1 \approx 140$ MeV and $T_2 \approx 230$ MeV. The value of T_1 is in close proximity to the freeze-out surface.

Considering the normalization of the initial entropy density, it can be seen that both values for *norm* are similar, while the value of τ_0 increases for the temperature dependent η/s. A larger value for τ_0 corresponds to a later development of pressure gradients within the medium and correspondingly a later initialization of the hydrodynamic evolution. The ratio $norm/\tau_0$, which is the normalizing factor of the initial entropy density, decreases for the temperature dependent η/s in comparison to the temperature independent η/s. This corresponds to a smaller initial entropy density for the temperature dependent η/s. Therefore, entropy production of the temperature dependent η/s and resulting particle production occurs more strongly during the hydrodynamic evolution in comparison to the temperature independent

η/s. The maxima of ζ/s appear to be similar for both models, which means that the influence of η/s on the particle spectra in different temperature regions can be compared between the two functional forms for η/s.
The scale-factor for the temperature dependent function lowers η/s to values below the constant value of the temperature independent η/s for temperatures above $T_1 = 140$ MeV, which is close to the freeze-out surface of both models. This could indicate that a major part of the particle production of the temperature dependent model for this parametrization (see table 2.1, second row) occurs during the high temperature phase of the system. However, further studies would need to be conducted in order to find conclusive results.

5 | Conclusion & Outlook

In this thesis a temperature dependent model for the transport coefficient η/s was implemented in a hydrodynamic simulation program called Fluidum. The effects of the temperature dependent model on particle spectra were investigated. The temperature dependent model was set to a constant value for certain temperature regions. With this it was demonstrated that the high and low temperature region of the temperature dependent model influence particle spectra to a similar extend. Furthermore, best-fit values were found for the temperature dependent and the temperature independent model by performing grid searches along the parameters $norm$, A / η/s, $(\zeta/s)_{max}$, τ_0 and T_{fo} and comparing the resulting particle spectra, calculated with Fluidum to experimental data from the ALICE experiment. Both models showed good agreement with the experimental data. It was found that the temperature independent model for η/s can describe the experimental data slightly better ($\chi^2_{red} = 1.19$) than the temperature dependent model for η/s ($\chi^2_{red} = 1.25$). However no decisive conclusions about the ability of the temperature dependent model to fit the experimental data can be drawn yet for various reasons (imprecise estimation of the χ^2_{red} by the spline, dependence on initialization and order of the spline). It could be found that the temperature dependent model was scaled by a factor of $A = 0.73$ for the best-fit configuration. Furthermore a slightly higher value of τ_0 in the best-fit parameters of the temperature dependent model lead to the conclusion of a slightly delayed hydrodynamic evolution and a lower initial entropy density.

Further investigations have to made in order to reach decisive conclusions. During the time of writing this thesis it was found that a bug was present in the Fluidum code. This bug corresponds to an extreme assumption on the bulk and shear corrections which enter in the calculation of the freeze-out surface. Therefore the derived results will be recalculated with a milder assumption on the out-of-equilibrium corrections and will be appended to this thesis. This bug could have an influence on the location and depth of minima found in the χ^2-landscape. Furthermore it is still

topic of research why pions are underestimated by the calculations of Fluidum. This could also have a significant influence on the ability of a model to fit the experimental data.
Furthermore the dependence of the minimum in the χ^2_{red}-landscape on the initialization or the order of the spline which is used to fit the landscape will be investigated. A new direction of investigation could also be to use different initial conditions or different models for the transport coefficient ζ/s. Moreover, other centrality classes could be investigated with this new temperature dependent η/s.

Bibliography

[1] A. Deur, S. J. Brodsky, and G. F. de Téramond, "The qcd running coupling," *Progress in Particle and Nuclear Physics*, vol. 90, p. 1–74, Sep 2016. [Online]. Available: http://dx.doi.org/10.1016/j.ppnp.2016.04.003

[2] M. e. a. Tanabashi, "Review of particle physics," *Phys. Rev. D*, vol. 98, p. 030001, Aug 2018. [Online]. Available: https://link.aps.org/doi/10.1103/PhysRevD.98.030001

[3] V. Gribov, "The theory of quark confinement," *The European Physical Journal C-Particles and Fields*, vol. 10, no. 1, pp. 91–105, 1999.

[4] R. Pasechnik and M. Šumbera, "Phenomenological review on quark–gluon plasma: Concepts vs. observations," *Universe*, vol. 3, no. 1, p. 7, 2017.

[5] B. Tomášik, J. Cimerman, R. Kopečná, and M. Schulc, "Fluctuating shapes of fireballs in heavy-ion collisions," *EPJ Web of Conferences*, vol. 204, p. 03011, 2019. [Online]. Available: http://dx.doi.org/10.1051/epjconf/201920403011

[6] D. V. Anchishkin and S. N. Yezhov, "Thermalization in Heavy-Ion Collisions," *Ukr. J. Phys.*, vol. 53, pp. 87–97, 2008.

[7] T. S. Biró, G. Purcsel, and B. Müller, "What is the temperature in heavy ion collisions?" *Acta Physica Hungarica A) Heavy Ion Physics*, vol. 21, no. 1, p. 85–94, Jul 2004. [Online]. Available: http://dx.doi.org/10.1556/APH.21.2004.1.9

[8] P. Braun-Munzinger, K. Redlich, and J. Stachel, "Particle production in heavy ion collisions," *Quark–Gluon Plasma 3*, p. 491–599, Jan 2004. [Online]. Available: http://dx.doi.org/10.1142/9789812795533_0008

[9] J. Casalderrey-Solana, H. Liu, D. Mateos, K. Rajagopal, and U. A. Wiedemann, *Gauge/string duality, hot QCD and heavy ion collisions*. Cambridge University Press, 2014.

[10] P. Romatschke and U. Romatschke, "Viscosity information from relativistic nuclear collisions: How perfect is the fluid observed at rhic?" *Physical Review Letters*, vol. 99, no. 17, Oct 2007. [Online]. Available: http://dx.doi.org/10.1103/PhysRevLett.99.172301

[11] A. Bazavov, H.-T. Ding, P. Hegde, O. Kaczmarek, F. Karsch, N. Karthik, E. Laermann, A. Lahiri, R. Larsen, S.-T. Li, and et al., "Chiral crossover in qcd at zero and non-zero chemical potentials," *Physics Letters B*, vol. 795, p. 15–21, Aug 2019. [Online]. Available: http://dx.doi.org/10.1016/j.physletb.2019.05.013

[12] P. Steinbrecher, "The qcd crossover at zero and non-zero baryon densities from lattice qcd," *Nuclear Physics A*, vol. 982, p. 847–850, Feb 2019. [Online]. Available: http://dx.doi.org/10.1016/j.nuclphysa.2018.08.025

[13] A. Jaiswal and V. Roy, "Relativistic hydrodynamics in heavy-ion collisions: General aspects and recent developments," *Advances in High Energy Physics*, vol. 2016, p. 1–39, 2016. [Online]. Available: http://dx.doi.org/10.1155/2016/9623034

[14] U. Heinz and G. Kestin, "Jozsó's legacy: Chemical and kinetic freeze-out in heavy-ion collisions," *The European Physical Journal Special Topics*, vol. 155, no. 1, p. 75–87, Mar 2008. [Online]. Available: http://dx.doi.org/10.1140/epjst/e2008-00591-4

[15] Vasileiou, Maria, "Identified charged hadron production in pp and pb-pb collisions with alice at the lhc," *EPJ Web Conf.*, vol. 126, p. 04052, 2016. [Online]. Available: https://doi.org/10.1051/epjconf/201612604052

[16] W. Busza, K. Rajagopal, and W. van der Schee, "Heavy ion collisions: The big picture and the big questions," *Annual Review of Nuclear and Particle Science*, vol. 68, no. 1, p. 339–376, Oct 2018. [Online]. Available: http://dx.doi.org/10.1146/annurev-nucl-101917-020852

[17] J. Berges, M. P. Heller, A. Mazeliauskas, and R. Venugopalan, "Thermalization in qcd: theoretical approaches, phenomenological applications, and interdisciplinary connections," 2020.

[18] L. Landau and E. Lifshitz, *Fluid Mechanics: Volume 6*. Elsevier Science, 2013, no. Bd. 6. [Online]. Available: https://books.google.de/books?id=CeBbAwAAQBAJ

[19] A. Bazavov, T. Bhattacharya, C. DeTar, H.-T. Ding, S. Gottlieb, R. Gupta, P. Hegde, U. Heller, F. Karsch, E. Laermann, and et al., "Equation of state in (2+1)-flavor qcd," *Physical Review D*, vol. 90, no. 9, Nov 2014. [Online]. Available: http://dx.doi.org/10.1103/PhysRevD.90.094503

[20] G. Kestin and U. Heinz, "Hydrodynamic radial and elliptic flow in heavy-ion collisions from ags to lhc energies," *The European Physical Journal C*, vol. 61, no. 4, p. 545–552, Dec 2008. [Online]. Available: http://dx.doi.org/10.1140/epjc/s10052-008-0832-y

[21] S. Floerchinger, E. Grossi, and J. Lion, "Fluid dynamics of heavy ion collisions with mode expansion," *Physical Review C*, vol. 100, no. 1, Jul 2019. [Online]. Available: http://dx.doi.org/10.1103/PhysRevC.100.014905

[22] P. Kovtun and A. Shukla, "Kubo formulas for thermodynamic transport coefficients," *Journal of High Energy Physics*, vol. 2018, no. 10, Oct 2018. [Online]. Available: http://dx.doi.org/10.1007/JHEP10(2018)007

[23] S. Plumari, A. Puglisi, F. Scardina, and V. Greco, "Shear viscosity of a strongly interacting system: Green-kubo correlator versus chapman-enskog and relaxation-time approximations," *Physical Review C*, vol. 86, no. 5, Nov 2012. [Online]. Available: http://dx.doi.org/10.1103/PhysRevC.86.054902

[24] N. Christiansen, M. Haas, J. M. Pawlowski, and N. Strodthoff, "Transport coefficients in yang-mills theory and qcd," *Physical Review Letters*, vol. 115, no. 11, Sep 2015. [Online]. Available: http://dx.doi.org/10.1103/PhysRevLett.115.112002

[25] P. K. Kovtun, D. T. Son, and A. O. Starinets, "Viscosity in strongly interacting quantum field theories from black hole physics," *Physical Review Letters*, vol. 94, no. 11, Mar 2005. [Online]. Available: http://dx.doi.org/10.1103/PhysRevLett.94.111601

[26] S. Cremonini, "The shear viscosity to entropy ratio: a status report," *Modern Physics Letters B*, vol. 25, no. 23, p. 1867–1888, Sep 2011. [Online]. Available: http://dx.doi.org/10.1142/S0217984911027315

[27] J. Rais, K. Gallmeister, and C. Greiner, "Shear viscosity to entropy density ratio of hagedorn states," *Physical Review D*, vol. 102, no. 3, Aug 2020. [Online]. Available: http://dx.doi.org/10.1103/PhysRevD.102.036009

[28] U. Heinz and R. Snellings, "Collective flow and viscosity in relativistic heavy-ion collisions," *Annual Review of Nuclear and Particle Science*, vol. 63, no. 1, p. 123–151, Oct 2013. [Online]. Available: http://dx.doi.org/10.1146/annurev-nucl-102212-170540

[29] D. Devetak, A. Dubla, S. Floerchinger, E. Grossi, S. Masciocchi, A. Mazeliauskas, and I. Selyuzhenkov, "Global fluid fits to identified particle transverse momentum spectra from heavy-ion collisions at the large hadron collider," *Journal of High Energy Physics*, vol. 2020, no. 6, 2020.

[30] H. Niemi, G. S. Denicol, P. Huovinen, E. Molnár, and D. H. Rischke, "Influence of shear viscosity of quark-gluon plasma on elliptic flow in ultrarelativistic heavy-ion collisions," *Physical Review Letters*, vol. 106, no. 21, May 2011. [Online]. Available: http://dx.doi.org/10.1103/PhysRevLett.106.212302

[31] P. Arnold, G. D. Moore, and L. G. Yaffe, "Transport coefficients in high temperature gauge theories (i): leading-log results," *Journal of High Energy Physics*, vol. 2000, no. 11, p. 001, 2000.

[32] L. P. Csernai, J. I. Kapusta, and L. D. McLerran, "Strongly interacting low-viscosity matter created in relativistic nuclear collisions," *Physical Review Letters*, vol. 97, no. 15, Oct 2006. [Online]. Available: http://dx.doi.org/10.1103/PhysRevLett.97.152303

[33] S. Ryu, J.-F. Paquet, C. Shen, G. Denicol, B. Schenke, S. Jeon, and C. Gale, "Effects of bulk viscosity and hadronic rescattering in heavy ion collisions at energies available at the bnl relativistic heavy ion collider and at the cern large hadron collider," *Physical Review C*, vol. 97, no. 3, Mar 2018. [Online]. Available: http://dx.doi.org/10.1103/PhysRevC.97.034910

[34] J. E. Bernhard, J. S. Moreland, S. A. Bass, J. Liu, and U. Heinz, "Applying bayesian parameter estimation to relativistic heavy-ion collisions: simultaneous characterization of the initial state and quark-gluon plasma medium," *Physical Review C*, vol. 94, no. 2, p. 024907, 2016.

[35] J. S. Moreland, J. E. Bernhard, and S. A. Bass, "Estimating initial state and quark-gluon plasma medium properties using a hybrid model with nucleon substructure calibrated to p-pb and pb-pb collisions at $\sqrt{s_{NN}} = 5.02$ tev," *arXiv preprint arXiv:1808.02106*, 2018.

[36] ——, "Alternative ansatz to wounded nucleon and binary collision scaling in high-energy nuclear collisions," *Physical Review C*, vol. 92, no. 1, Jul 2015. [Online]. Available: http://dx.doi.org/10.1103/PhysRevC.92.011901

[37] B. Abelev, J. Adam, D. Adamová, A. M. Adare, M. M. Aggarwal, G. Aglieri Rinella, M. Agnello, A. G. Agocs, A. Agostinelli, Z. Ahammed, and et al., "Centrality determination of pb-pb collisions at $\sqrt{s_{NN}} = 2.76$ tev with alice," *Physical Review C*, vol. 88, no. 4, Oct 2013. [Online]. Available: http://dx.doi.org/10.1103/PhysRevC.88.044909

[38] M. L. Miller, K. Reygers, S. J. Sanders, and P. Steinberg, "Glauber modeling in high-energy nuclear collisions," *Annual Review of Nuclear and Particle Science*, vol. 57, no. 1, p. 205–243, Nov 2007. [Online]. Available: http://dx.doi.org/10.1146/annurev.nucl.57.090506.123020

[39] F. Cooper and G. Frye, "Single-particle distribution in the hydrodynamic and statistical thermodynamic models of multiparticle production," *Phys. Rev. D*, vol. 10, pp. 186–189, Jul 1974. [Online]. Available: https://link.aps.org/doi/10.1103/PhysRevD.10.186

[40] D. Teaney, "Effect of shear viscosity on spectra, elliptic flow, and hanbury brown–twiss radii," *Phys. Rev. C*, vol. 68, p. 034913, Sep 2003. [Online]. Available: https://link.aps.org/doi/10.1103/PhysRevC.68.034913

[41] A. Mazeliauskas, S. Floerchinger, E. Grossi, and D. Teaney, "Fast resonance decays in nuclear collisions," *The European Physical Journal C*, vol. 79, no. 3, Mar 2019. [Online]. Available: http://dx.doi.org/10.1140/epjc/s10052-019-6791-7

[42] K. Olive, "Review of particle physics," *Chinese Physics C*, vol. 40, no. 10, p. 100001, oct 2016. [Online]. Available: https://doi.org/10.1088%2F1674-1137%2F40%2F10%2F100001

[43] B. Abelev, J. Adam, D. Adamová, A. M. Adare, M. M. Aggarwal, G. Aglieri Rinella, M. Agnello, A. G. Agocs, A. Agostinelli, Z. Ahammed, and et al., "Centrality dependence of π ,k, and p production in pb-pb collisions at $\sqrt{s_N N} = 2.76$tev," *Physical Review C*, vol. 88, no. 4, Oct 2013. [Online]. Available: http://dx.doi.org/10.1103/PhysRevC.88.044910

[44] F. James, "MINUIT Function Minimization and Error Analysis: Reference Manual Version 94.1," 1994.